

Experimental Evidence of Stable 2H Phase on the Surface of Layered 1T'-TaTe₂

Indrani Kar,[†] Kapildeb Dolui,[‡] Luminita Harnagea,[¶] Y. Kushnirenko,[§] G. Shipunov,[§] N. C. Plumb,^{||} M. Shi,^{||} B. Büchner,[§] and S. Thirupathaiah^{*,†}

[†]*Department of Condensed Matter Physics and Material Sciences, S N Bose National Centre for Basic Sciences, Kolkata, West Bengal-700106, India.*

[‡]*Department of Physics and Astronomy, University of Delaware, Newark, DE 19716, USA*

[¶]*Indian Institute of Science Education and Research, Dr. Homi Bhabha Road, Pune, Maharashtra-411008, India.*

[§]*Leibniz-Institute for Solid State and Materials Research Dresden, P.O.Box 270116, D-01171 Dresden, Germany.*

^{||}*Swiss Light Source, Paul Scherrer Institute, CH-5232 Villigen PSI, Switzerland.*

E-mail: setti@bose.res.in

Abstract

We report on the low-energy electronic structure of Tantalum ditelluride (1T'-TaTe₂), one of the charge density wave (CDW) materials from the group V transition metal dichalcogenides using angle-resolved photoemission spectroscopy (ARPES) and density functional theory (DFT). We find that the Fermi surface topology of TaTe₂ is quite complicated compared to its isovalent compounds such as TaS₂, TaSe₂, and isostructural compound NbTe₂. More importantly, we discover that the surface electronic structure of 1T'-TaTe₂ has more resemblance to the 2H-TaTe₂, while the bulk electronic structure has more resemblance to the hypothetical 1T-TaTe₂. These experimental observations are thoroughly compared with our DFT calculations performed

on $1T$ -, $2H$ - and $2H$ (monolayer)/ $1T$ - TaTe_2 . We further notice that the Fermi surface topology is temperature independent up to 180 K, confirming that the $2H$ phase on the surface is stable up to 180 K and the CDW order is not due to the Fermi surface nesting.

Investigation of the transition metal dichalcogenides (TMDCs) is quite fascinating as these systems host a wide variety of structural, physical, and electronic properties.¹⁻⁴ Particularly, the structural polymorphism in TMDCs ($1T$, $2H$, and $3R$ phases) play a significant role for their exotic physical properties such as charge density wave (CDW),^{5,6} superconductivity,⁷ magnetic ordering,⁸ topological properties,⁹ and the valleytronics¹⁰ by tuning the electronic band structure. Therefore, a thorough knowledge on the electronic band structure of TMDCs is vital for understanding their diverse electronic and physical properties.

TMDCs are in general formed by one transition metal atom (group IV, V, VI, VII, IX, and X) and two chalcogen atoms (S, Se, and Te) with the chemical formula of MX_2 ($\text{M}=\text{transition metal}$ and $\text{X}=\text{chalcogen}$). Among these, the group V TMDCs, NbX_2 and TaX_2 are most attractive as they show interplay between the charge ordering (CDW) and the superconductivity both in the $1T$ and $2H$ phases.¹¹ The mechanism of charge ordering and the superconductivity in TMDCs are under debate. Fermi surface nesting,¹² electron-phonon coupling,¹³ and the van Hove singularities¹⁴ have been proposed as the origin of CDW ordering in these systems.¹⁵ Though, the electronic properties are almost similar in both NbX_2 and TaX_2 , their structural properties are rather different. That means, at room temperature, the bulk $\text{Ta}(\text{Nb})\text{S}_2$ and $\text{Ta}(\text{Nb})\text{Se}_2$ can be formed in the $1T$ and $2H$ phases with octahedral and trigonal prismatic coordination in the hexagonal crystal symmetry⁴ having $(\sqrt{13} \times \sqrt{13})$ superstructure on the surface,¹⁶ while the bulk TaTe_2 and NbTe_2 are in the distorted octahedral coordination with the monoclinic crystal symmetry ($1T'$ phase) having (1×3) superstructure on the surface.¹⁷ Also at low temperatures, the surface of $\text{Ta}(\text{Nb})\text{Te}_2$ goes into the (3×3) superstructure with $1T'$ phase intact.¹⁸⁻²⁰ Further, TaTe_2 shows incommensurate CDW phase below $T_{CDW} \approx 170\text{K}$.^{13,18,19,21} whereas NbTe_2 shows commensurate

CDW order at room temperature but then turns into incommensurate CDW phase just above the room temperature.^{22,23}

So far TaTe₂ and NbTe₂ are experimentally studied for their structural,^{5,13,17,24} physical properties,^{18,20} magnetic properties,²⁵ and potential applications in the energy storage materials.^{26–28} Further, unlike TaTe₂ which does not show superconductivity down to lowest possible temperature, NbTe₂ shows superconductivity below $\approx 0.5K$.²⁹ Several theoretical calculations were performed to understand their structural transition and origin of CDW in these systems by studying the electronic band structure using the DFT calculations .^{13,16,20} However, till date, one experimental ARPES report available on NbTe₂²² and none on TaTe₂. But one quantum oscillation study discussing the speculative band structure of TaTe₂ is available.²⁵ Since ARPES studies are utmost needed to unambiguously understand the low-energy electronic structure of these systems, we performed ultra-high resolution ARPES studies on TaTe₂ to understand the origin of CDW transition and to examine whether it is a Dirac semimetal as speculated by the quantum oscillations.²⁵

In this study, we report on the low-energy electronic structure of 1T'-TaTe₂ using high-resolution angle-resolved photoemission spectroscopy (ARPES) and density functional theory calculations. We observe that the Fermi surface of 1T'-TaTe₂ is in the hexagonal symmetry, which is in contradiction to its monoclinic crystal structure. We observe a totally different electronic structure of TaTe₂ when compared with the isostructural compound NbTe₂. Further, despite being in the hexagonal symmetry the Fermi surface topology of TaTe₂ is quite different when compared to the isovalent compounds, TaSe₂ and TaS₂. To fully understand the experimentally obtained electronic band structure of TaTe₂, we disentangled the surface states from bulk with the help of the slab calculations. Thus, we realize that the surface states resemble the 2H phase electronic structure, while the bulk states replicate the 1T phase electronic structure of TaTe₂. This is an interesting discovery as TaTe₂ does exist neither in 1T phase nor in 2H phase as per the observation of crystal structure. We further notice that the 1T phase electronic structure shows substantial band dispersion in

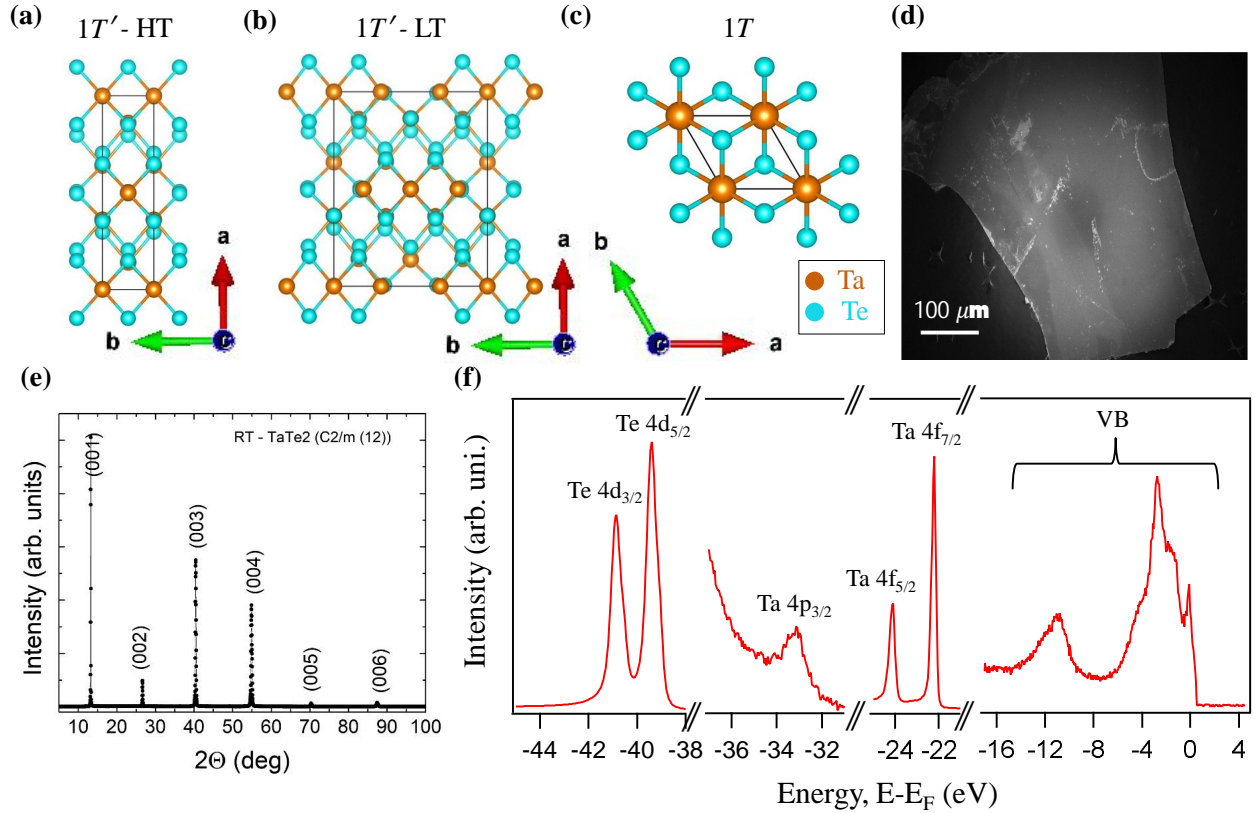


Figure 1: Distorted 1T phase (1T') or the monoclinic crystal structure of TaTe₂ at high temperature (a) and at low temperature (b). (c) Hypothetical 1T phase crystal structure of TaTe₂ projected onto the ab-plane. (d) Scanning electron microscope image of the 1T'-TaTe₂ single crystal. (e) X-ray diffractogram of 1T'-TaTe₂ single crystal. (f) X-ray photoemission spectra (XPS) measured with a photon energy of 100 eV. On the XPS, all core levels are identified either to Ta or Te atom.

the k_z direction. We realize that the band structure of TaTe_2 is temperature independent above and below the CDW transition temperature.

Results and discussion

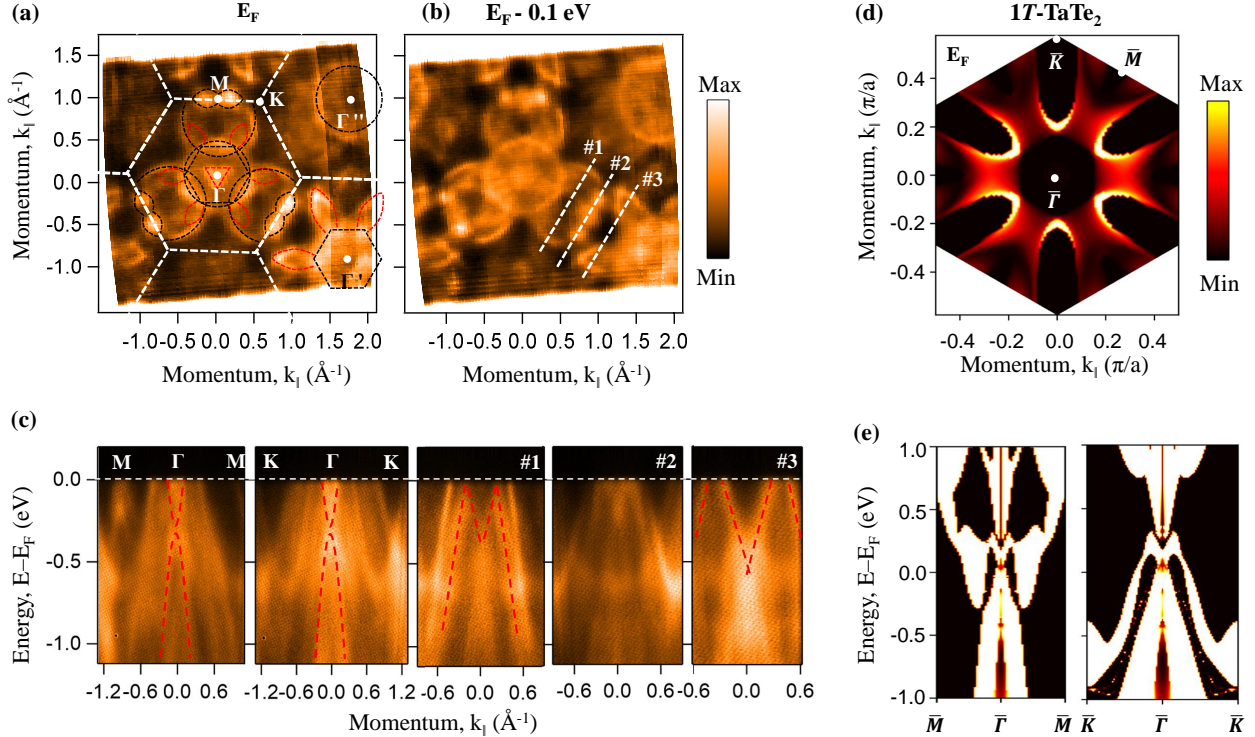


Figure 2: In-plane Fermi surface topology of TaTe_2 measured at a sample temperature of 1 K. (a) and (b) show the constant energy contours at the Fermi level and 100 meV below the Fermi level, respectively measured with a photon energy $h\nu = 100 \text{ eV}$. (c) Energy-momentum distribution maps (EDMs) taken along $\Gamma-K$, $\Gamma-M$, and along the cuts #1-#3 as shown in (b). (d) Constant energy contour of the spectral function intensity at the Fermi level derived from the DFT calculations performed on the semi-infinite $1T$ - TaTe_2 slab. (e) Spectral function distribution of the energy-momentum plot along the high-symmetry lines $\bar{\Gamma}M$ and $\bar{\Gamma}K$.

The crystal structure of TaTe_2 in the $1T'$ phase with monoclinic crystal symmetry is shown in **Figure 1a** at high temperature ($T > 170\text{K}$) and in **Figure 1b** at low temperature ($T < 170\text{K}$) reproduced from Ref.¹⁸ As can be seen from **Figures 1a and b** the crystal symmetry does not change but only the lattice constants do alter above and below the CDW order transition temperature ($T \approx 170\text{K}$). **Figure 1c** shows the hypothetical crystal structure

of TaTe_2 in the $1T$ phase with the hexagonal crystal symmetry projected onto the ab plane. Scanning electron microscope (SEM) image of TaTe_2 single crystal is shown in **Figure 1d**. From the energy dispersive x-ray analysis spectroscopy (EDS) measurements (see **Figure S1** in supporting information), we derived the chemical composition as $\text{Ta}_{1.06}\text{Te}_2$. This suggests that there exists a 6% of excess Ta per unit cell. Such an excess amount of transition metal or chalcogen deficiency in these systems generally leads to excess electron carrier density. Otherwise, from the EDS and SEM data the sample is noticed as homogeneous. **Figure 1e** shows X-ray diffraction (XRD) pattern, measured at room temperature, indicating that TaTe_2 single crystal is crystallized in the space group of $C2/m(12)$, with lattice parameters as $a = 14.76 \text{ \AA}$, $b = 3.63 \text{ \AA}$, $c = 9.32 \text{ \AA}$, and $\beta = 110.89^\circ$. The crystal surface normal is parallel to the c -axis, analogous to the earlier reports.^{20,25} Also, we performed XPS measurements on the cleaved TaTe_2 to check the purity of the sample, before performing the ARPES measurements as shown in **Figure 1f**. All observed core levels from XPS are referred to respective binding energies of Ta and Te atoms and no other impurity peaks are detected.

Fermi surface topology of TaTe_2 in the k_x - k_y plane is shown in **Figure 2a**, measured with a photon energy of 100 eV using p -polarized light at a sample temperature of 1K. **Figure 2b** depicts constant energy contour taken at a binding energy of 100 meV below the Fermi level. As can be seen from the maps, the Fermi sheets follow the hexagonal symmetry that is in contrast to its monoclinic crystal structure as observed from the XRD measurements (**Figure 1e**). The symmetry difference between the crystal and electronic structures could be related to the formation of bulk $(3 \times 1 \times 3)$ supercell structure as reported earlier in the case of isostructural $1T'$ - NbTe_2 .²² Further, on the Fermi surface map, we could identify various Fermi pockets of circular-shaped, hexagonal-shaped, petal-shaped, half-circular-shaped, and triangular-shaped. In detail, at the Γ point we see a large circular-shaped Fermi pocket. Though we identify another large hexagonal-shaped Fermi pocket at the Γ point, due to the matrix element effects it is not very clear. But this hexagonal-shaped Fermi pocket is clearly visible as we move to the Γ' point. Further, at the Γ point we do find six petal-shaped, three

half-circle-shaped and one triangular-shaped Fermi pockets. Interestingly, as we move away from Γ to the Γ' point we find large hexagonal-shaped Fermi pocket that is not clear at the Γ point. Also, at Γ' , the size of the petal-shaped Fermi pockets is significantly enhanced compared to their size at Γ . We did not observe any half-circle-shaped Fermi pockets at Γ' . Next, at Γ'' , we could readily observe one circular-shaped Fermi pocket of the same size to the one at Γ and with a careful observation we could also find the half-circular-shaped Fermi pockets. At the M point, we observe peanut-shaped Fermi pocket. Due to the matrix element effects out of six peanut-shaped Fermi pockets, only three are readily visible due to their high spectral intensity and the other three peanut-shaped pockets exist with reduced spectral intensity.

To elucidate the nature of band dispersions contributing to the Fermi pockets, we plotted the energy distribution maps (EDMs) taken along ΓK , ΓM , #1, #2, and #3 directions as shown in **Figure 2c**. From these EDMs one can realize that at the Γ point the triangular shapedd Fermi sheet has an electronlike band dispersion, while the larger circular- and hexagonal-shaped Fermi sheets have the holelike band dispersions. From the EDM cut #1 we can see that the petal-shaped and half-circle-shaped Fermi sheets have the holelike band dispersions. Similarly, from the EDM cut #2 we find that the peanut-shaped Fermi sheet at the M point has the holelike band dispersions. Next, the EDM cut #3 identifies holelike band dispersion for the petal-shaped Fermi sheet corresponding to Γ' . Note here that the Fermi vector of the petal-shaped hole pocket is negligible at Γ as it does not cross the Fermi level, however, it has a finite Fermi vector of 0.1^{-1} near the Γ' point. Therefore, the petal-shaped hole pocket has significant k_z dispersion, must be originating from the bulk band structure. Similarly, the triangular-shaped hole pocket at Γ totally disappears at Γ' which is possible only if it is of the bulk nature. Thus, from our experimental data we can unambiguously conclude that the petal-shaped and triangular-shaped Fermi sheets are originated from the bulk bands, while the rest of Fermi sheets are originated from the surface bands.

As the ARPES is a surface sensitive technique, inevitably, it probes the surface electronic

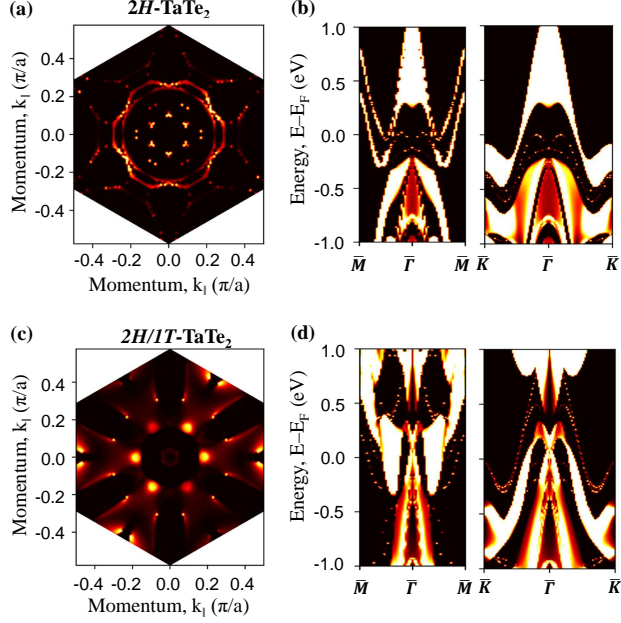


Figure 3: Constant energy contours of the spectral function distribution at the Fermi level plotted for (a) semi-infinite slab of 2H-TaTe₂ and (b) Spectral function distribution of the energy-momentum plot along the high-symmetry lines $\overline{\Gamma M}$ and $\overline{\Gamma K}$. (c) and (d) are same as (a) and (b) but plotted for the system, 2H-TaTe₂ monolayer placed on top of the semi-infinite 1T-TaTe₂ slab.

structure in addition to the bulk electronic structure. Therefore, it is crucial to disentangle the surface electronic structure from the bulk resulted from the surface reconstruction due to crystal cleavage under ultra-high chamber vacuum. For this purpose, we performed slab calculations of TaTe₂ in its 1T-phase, 2H-phase, and 2H-phase monolayer on top of the bulk 1T-phase (hybrid-phase) TaTe₂ have been performed using the density functional theory following the Eqn. 2. **Figure 2d** is the spectral function intensity plot in the k_x - k_y plane at the Fermi level (from the top surface layer of the semi-infinite slab). **Figure 2e** represents energy-momentum plot along the $\overline{\Gamma M}$ and $\overline{\Gamma K}$ high symmetry directions. **Figure 3a** presents the spectral function intensity plot of the 2H-phase TaTe₂ in the k_x - k_y plane at the Fermi level. **Figure 3b** shows energy-momentum plot along the $\overline{\Gamma M}$ and $\overline{\Gamma K}$ directions. **Figure 3c** presents the spectral function intensity plot of hybrid-phase TaTe₂ in the k_x - k_y plane at the Fermi level. **Figure 3d** shows energy-momentum plot of hybrid-phase along the $\overline{\Gamma M}$ and $\overline{\Gamma K}$ directions.

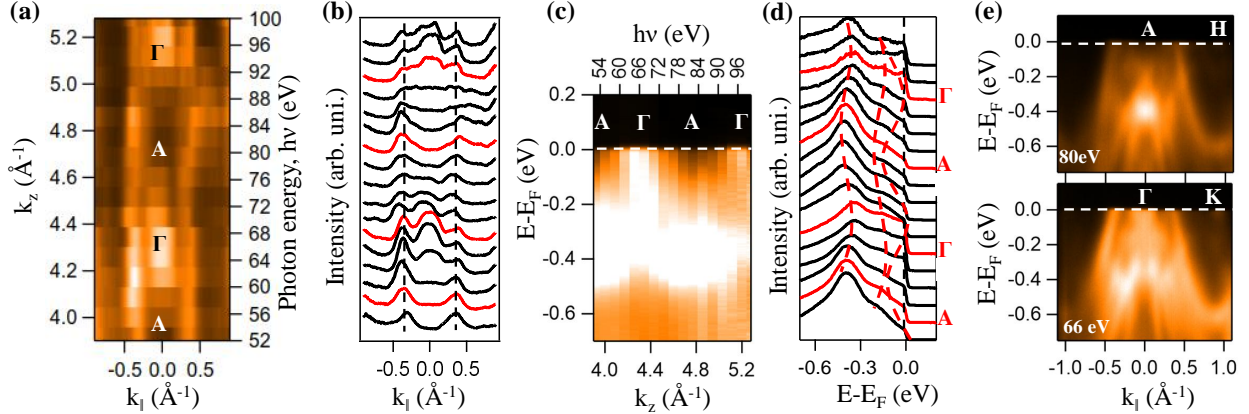


Figure 4: Out-of-plane (k_z) electronic structure of TaTe_2 measured at 1K. (a) k_z Fermi surface map in $\Gamma K H A$ plane. (b) Photon energy dependent momentum distribution curves extracted from (a). (c) Energy distribution map (EDM) taken along the Γ - A high symmetry line. (d) Photon energy dependent energy distribution curves extracted from (c). (e) EDMs taken from Γ - K and A - H high symmetry lines.

On comparing the experimental data presented in **Figures 2a-c** with the slab calculations presented in **Figures 2(d,e), 3**, we can find that there is a qualitative agreement to some extent between experiment and theory. For instance, the circular-shaped and half-circular-shaped hole pockets are reproduced from the $2H$ -phase. The peanut-shaped hole pocket can be noticed very well from the hybrid-phase, though we can see it from the $1T$ -phase with reduced intensity. Next, the hexagonal-shaped hole pocket is visible only in the hybrid-phase. Nevertheless, the triangular-shaped electron pocket and the petal-shaped hole pockets are not visible from any of these slab calculations, could be due to their bulk origin.

Figure 4 shows out-of-plane (k_z) ARPES measurements on TaTe_2 . **Figure 4a** shows k_z Fermi surface map in k_{\parallel} - k_z plane measured with photon energy ranging from 52 to 100 eV with a step of 3 eV. High symmetry points Γ and A are located on the k_z map. **Figure 4b** depicts the photon energy dependent momentum distribution curves (MDCs). From **Figure 4b** we can notice mainly three peaks, out of which two peaks (shown by the vertical-dashed lines) always present irrespective of the applied photon energy while the middle-peak appears significantly at the photon energies of 66 and 94 eV and then the peak intensity gradually decreases as we move away from these photon energies to totally disappear at

photon energies 52 and 80 eV. **Figure 4c** shows EDM taken along the Γ - A direction. From **Figure 4c** we can notice that the band is crossing the Fermi level near Γ . Observation of the experimental k_z dispersions along the Γ - A high symmetry line are in very good agreement with the bulk band structure calculations of 1T-TaTe₂ (see **Figure S3** in the supplemental). **Figure 4d** shows energy distribution curves (EDCs) extracted from the EDM shown in **Figure 4c**. EDMs along Γ - K and A - H orientation are shown in **Figure 4e**. Following the equation $k_z = \sqrt{\frac{2m}{\hbar^2}(V_0 + E_k \cos^2 \theta)}$ and considering the inner potential $V_0 = 11 \pm 2$ eV with a lattice constant $c = 9.30$ of low temperature,¹⁸ we identified that the Γ point can be probed with photon energies $h\nu = 66$ and 92 eV, while the A point can be probed with photon energies 54 and 80 eV. Here, m is the rest mass of electron, \hbar is the PlanckâŽs constant, E_k is the photoelectron kinetic energy, and θ is photoelectron emission angle with respect to the sample surface normal.

Since TaTe₂ shows CDW order at 170 K,¹¹ we have measured the ARPES data above and below the CDW transition temperature to understand the effect of electronic band structure on the CDW order. **Figure 5** shows the Fermi surface (FS) maps measured with 100 eV photon energy using p polarized light. Left panel in **Figure 5** shows the FS map measured at a sample temperature of 20 K, middle panel is the FS map measured at 180 K, and right panel is the FS map measured at 20 K immediately after cooling down from 180 K. As can be noticed from **Figure 5**, the FS topology hardly changes across the CDW transition temperature, except that over a full temperature cycle the spectral intensity reduced for the

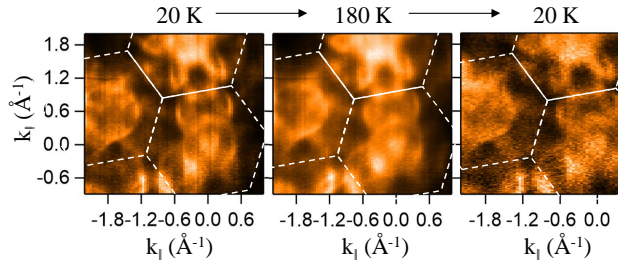


Figure 5: Temperature dependent Fermi surface (FS) topology of TaTe₂. FS measured at 20 K (left), 180 K (middle), and 20 K after cooling down from 180 K (right).

surface states (see right panel) due to sample aging.

Next, we compare the experimental band structure of TaTe₂ with the existing literature on the isovalent compounds like, 1T-TaS₂, 1T-TaSe₂ and the isostructural compound 1T'-NbTe₂. Despite being the FS topology of these compounds in the hexagonal symmetry we do not find any qualitative agreement with TaTe₂. We identify one circular-shaped and one hexagonal-shaped hole pockets at the Γ point from TaTe₂, whereas no such circular-shaped hole pockets have been found from 1T-TaS₂,³⁰ 1T-TaSe₂,^{31,32} and 1T'-NbTe₂.²² However, the petal-shaped hole pocket noticed in 1T'-TaTe₂ is consistent with these systems. Further, the electronic band dispersions of TaTe₂ do neither agree with TaSe₂ nor with TaS₂ which are formed by the isovalent substitution of Se/S at the Te site. This is rare to find drastic changes in the electronic structure by isovalently replacing the chalcogen atom in the TMDCs. It is known that a relative shifting of the valance and conduction bands with isovalent substitution takes place.⁹ Hence, understanding the electronic structure of TaTe₂ has become very complex by simply comparing with the 1T-phase of the other similar systems. Importantly, we notice from the total energy calculation of slab 1T-TaTe₂ (20 monolayers) that the top surface layer of 1T-TaTe₂ favourably transforms into the 2H-phase. Moreover, the calculated spectral function of the stand alone 2H phase monolayer and the 2H phase surface monolayer on top of the semi-infinite 1T- phase slab, matches quite well with our ARPES data. In addition, our ARPES data qualitatively agree with the ARPES data of 2H-TaSe₂^{33,34} and 2H-TaS₂³⁵ where one can find the circular-shaped, half-circular-shaped, and hexagonal-shaped hole pockets at the Γ point. Therefore, the surface states observed on top of the bulk 1T'-TaTe₂ from our studies are originated by the surface reconstruction to form 2H-TaTe₂.

Finally, we notice that the band structure of TaTe₂ hardly changes across the CDW transition temperature ($T_{CDW} \approx 170\text{K}$) as shown in **Figure 5**, thus, ruling out the Fermi surface nesting mechanism as the origin of CDW ordering in this system. Perhaps, the electron-phonon scattering could be the reason for CDW phase in TaTe₂ as discussed in

the previous reports.^{16,22} Also, it is worth to mention here that the $2H$ -phase surface layer is stable even after raising the sample temperature up to 180 K and moving to back 20 K as the Fermi surface topology does not change much with the temperature. An earlier quantum oscillations study on TaTe_2 suggested the presence of topological Dirac cone in this system.²⁵ But from our systematic ARPES measurements and DFT calculations, we do not observe any signature of the suggested Dirac cone. On the other hand, some of the transport studies on TaTe_2 reported it to be a semimetal.^{25,36,37} Our experimental studies qualitatively support this argument, if we ignore the large number of surface states, as we observe a bulk triangular-shaped electron pocket at the Γ point and six petal-shaped hole pockets surrounding it.

Conclusions

In conclusion, we have systematically studied the low-energy electronic structure of layered Tantalum ditelluride ($1T'$ - TaTe_2) using angle-resolved photoemission spectroscopy and density functional theory. We find that the Fermi surface topology of TaTe_2 is rather different when compared to the isostructural compounds of TaTe_2 such as TaS_2 , TaSe_2 , and NbTe_2 . Interestingly, we realize that the surface electronic structure of $1T'$ - TaTe_2 has more resemblance to the $2H$ - TaTe_2 , while the bulk electronic structure $1T'$ - TaTe_2 has more resemblance to the $1T$ - TaTe_2 . These experimental observations are systematically compared with our DFT calculations performed on $1T$ -, $2H$ - and $2H$ (monolayer)/ $1T$ - TaTe_2 . We further notice that the Fermi surface topology is temperature independent up to 180 K, confirming that $2H$ phase on the top layer is very stable and the CDW order is not due to the Fermi surface nesting. Further, our studies do not show any evidence on the presence of Dirac cone in this system, though, leaving out the large number surface states and considering only the bulk states, we suggest that this system can be a semimetal.

Methods

Single Crystal Growth

The sample preparation and storage were carried out in an Ar-filled glove box where the moisture and oxygen is maintained below 0.1 ppm. Polycrystalline sample of TaTe₂, obtained by reacting stoichiometric amounts of Ta powder (Sigma Aldrich , 99.9%, metals basis) and Te (ingot, 99.99%, metals basis, Alfa Aesar) under vacuum (10^{-5} Torr) at 750° C for 48 h, was used for the single crystal growth. The polycrystalline sample was then grinded in glove box, loaded and sealed under vacuum in a quartz ampoule together with the transporting agent (iodine \approx 5 mg/cm³). Subsequently, the ampoule has been placed in a furnace with a gradient temperature between 870° C (source zone \approx T₁) and 820° C (sink zone \approx T₂). After 12 days, platelet shaped single crystals with a typical lateral dimensions of 10-15 mm were obtained.

Sample Characterization

The chemical purity and composition were confirmed using a scanning electron microscope (ZEISS Gemini SEM 500) equipped with an energy dispersive X-ray spectroscopy (EDX) probe. The phase purity of the single crystal was checked using X-ray diffraction (Bruker D8 diffractometer, Cu K α radiation) measurements.

ARPES measurements

ARPES measurements were carried out at 1³-ARPES end station using UE112-PGM2b beamline equipped with a Scienta R4000 analyzer having angular resolution better than 0.2° located in BESSY II (Helmholtz zentrum Berlin) synchrotron radiation center.^{38,39} Photon energies for the measurements were varied between 50 to 100 eV. The energy resolution was set between 5 and 15 meV depending on the excitation energy. Data were recorded at a chamber vacuum better than 1×10^{-10} mbar. Sample was cleaved *in situ* before the measure-

ments. The sample temperature was kept at 1 K during the measurements. Temperature dependent ARPES data were recorded at the SIS beamline located in Swiss Light Source⁴⁰ equipped with a Scienta R4000 electron analyzer with an angular resolution of better than 0.2°. The energy resolution was set at 10 meV. The sample was cleaved *in situ* before performing the measurements. The base pressure was better than 1×10^{-10} mbar during the measurements.

Theoretical Calculations

Our first-principles electronic structure calculations are performed within the framework of density functional theory (DFT) using the local density approximation (LDA)⁴¹ of the exchange and correlation (XC) functional as implemented in the Vienna Ab-initio Simulation Package (VASP).⁴² The projector augmented wave (PAW)⁴³ pseudo-potentials are used to describe the core electrons. Electronic wave-functions are expanded using plane waves up-to a cut-off energy of 600 eV. Periodic boundary conditions are employed and at least of 15 Å slab is used on the surface of few layers to eliminate the interaction between consecutive periodic images. The Monkhorst-Pack k-meshes are set to 11×11 ($11 \times 11 \times 4$) in the Brillouin zone for the self-consistent calculation of few layer cases (bulk), and all atoms are relaxed in each optimization cycle until atomic forces on each atom are smaller than 0.01 eV/Å. Spectral function is calculated using the QuantumATK package⁴⁴ where we use the VASP-relaxed structure, LDA XC functional, norm-conserving pseudopotentials for describing electron-core interactions, and SG15 (medium) type local orbital basis set.⁴⁵ The energy mesh cut-off for the real-space grid is chosen as 100 hartree. We obtain the spectral function at an arbitrary plane at position z within the heterostructure from the retarded GreenâŽs function, $G_{k\parallel}$

$$A(E = E_F; k_x, k_y) = \frac{1}{\pi} G_{k\parallel}(E; z.z), \quad (1)$$

and $G_{k\parallel}$ is calculated as

$$G_{k\parallel}(E) = [E - H_{k\parallel} - \Sigma_{k\parallel}]^{-1} \quad (2)$$

Here k_{\parallel} refers to the in-plane (k_x, k_y) k-points, $H_{k\parallel}$ is the DFT hamiltonian of the slab and Σ is the self energy of the semi-infinite lead

Author Information

Corresponding Author

E-mail: setti@bose.res.in (S.T.).

ORCID

Indrani Kar: 0000-0002-8478-2948

Luminita Harnagea: 0000-0002-6631-4403

S. Thirupathaiah: 0000-0003-1258-0981

Acknowledgements

L.H acknowledges the Department of Science and Technology (DST), India for the financial support through the Grant No. SR/WOS-A/PM-33/2018 (G). S.T. acknowledges support by the DST, India through the INSPIRE-Faculty program (Grant No. IFA14 PH-86). S.T. greatly acknowledges the financial support given by SNBNCBS through the Faculty Seed Grants program. This work was supported by the DFG under the Grant No. BO 1912/7-1. The supercomputing time is facilitated by the Chimera cluster at the University of Delaware, USA.

Conflicts of Interest

The authors declare no conflicts of interest.

Supporting Information Available

The following files are available free of charge. EDX measurements, additional ARPES data and bulk DFT calculations of TaTe₂ in 1T and 2H phase are shown in the supplemental information.

References

- (1) Guo, H.; Lu, N.; Wang, L.; Wu, X.; Zeng, X. C. Tuning Electronic and Magnetic Properties of Early Transition-Metal Dichalcogenides via Tensile Strain. *The Journal of Physical Chemistry C* **2014**, *118*, 7242–7249.
- (2) Wang, H.; Yuan, H.; Sae Hong, S.; Li, Y.; Cui, Y. Physical and chemical tuning of two-dimensional transition metal dichalcogenides. *Chem. Soc. Rev.* **2015**, *44*, 2664–2680.
- (3) Voiry, D.; Mohite, A.; Chhowalla, M. Phase engineering of transition metal dichalcogenides. *Chem. Soc. Rev.* **2015**, *44*, 2702–2712.
- (4) Manzeli, S.; Ovchinnikov, D.; Pasquier, D.; Yazyev, O. V.; Kis, A. 2D transition metal dichalcogenides. *Nature Reviews Materials* **2017**, *2*, 17033.
- (5) Luo, H.; Xie, W.; Tao, J.; Inoue, H.; Gyenis, A.; Krizan, J. W.; Yazdani, A.; Zhu, Y.; Cava, R. J. Polytypism, polymorphism, and superconductivity in TaSe_{2-x}Tex. *Proceedings of the National Academy of Sciences* **2015**, *112*, E1174–E1180.
- (6) Yoshida, M.; Ye, J.; Zhang, Y.; Imai, Y.; Kimura, S.; Fujiwara, A.; Nishizaki, T.;

Kobayashi, N.; Nakano, M.; Iwasa, Y. Extended Polymorphism of Two-Dimensional Material. *Nano Lett.* **2017**, *17*, 5567–5571.

(7) Sipos, B.; Kusmartseva, A. F.; Akrap, A.; Berger, H.; Forró, L.; Tutiš, E. From Mott state to superconductivity in 1T-TaS₂. *Nat. Mater.* **2008**, *7*, 960–965.

(8) Ma, Y.; Dai, Y.; Guo, M.; Niu, C.; Zhu, Y.; Huang, B. Evidence of the Existence of Magnetism in Pristine VX₂ Monolayers (X = S, Se) and Their Strain-Induced Tunable Magnetic Properties. *ACS Nano* **2012**, *6*, 1695–1701.

(9) Kar, I.; Chatterjee, J.; Harnagea, L.; Kushnirenko, Y.; Fedorov, A. V.; Shrivastava, D.; Büchner, B.; Mahadevan, P.; Thirupathaiah, S. Metal-chalcogen bond-length induced electronic phase transition from semiconductor to topological semimetal in ZrX₂ (X = Se and Te). *Phys. Rev. B* **2020**, *101*, 165122.

(10) Schaibley, J. R.; Yu, H.; Clark, G.; Rivera, P.; Ross, J. S.; Seyler, K. L.; Yao, W.; Xu, X. Valleytronics in 2D materials. *Nature Reviews Materials* **2016**, *1*, 16055.

(11) Chhowalla, M.; Shin, H. S.; Eda, G.; Li, L.-J.; Loh, K. P.; Zhang, H. The chemistry of two-dimensional layered transition metal dichalcogenide nanosheets. *Nat. Chem.* **2013**, *5*, 263–275.

(12) Johannes, M. D.; Mazin, I. I. Fermi surface nesting and the origin of charge density waves in metals. *Phys. Rev. B* **2008**, *77*, 165135.

(13) Liu, Y. et al. Nature of charge density waves and superconductivity in 1T-TaSe_{2-x}Tex. *Physical Review B* **2016**, *94*, 045131.

(14) Rice, T. M.; Scott, G. K. New Mechanism for a Charge-Density-Wave Instability. *Phys. Rev. Lett.* **1975**, *35*, 120–123.

(15) Barja, S. et al. Charge density wave order in 1D mirror twin boundaries of single-layer MoSe₂. *Nat. Phys.* **2016**, *12*, 751–756.

(16) Sharma, S.; Nordström, L.; Johansson, B. Stabilization of charge-density waves in 1T-TaX₂(X=S,Se,Te):First-principles total energy calculations. *Physical Review B* **2002**, *66*, 195101.

(17) Brown, B. E. The crystal structures of NbT₂and TaTe₂. *Acta Crystallographica* **1966**, *20*, 264–267.

(18) Sörgel, T.; Nuss, J.; Wedig, U.; Kremer, R. K.; Jansen, M. A new low temperature modification of TaTe₂—Comparison to the room temperature and the hypothetical 1T-TaTe₂ modification. *Materials Research Bulletin* **2006**, *41*, 987–1000.

(19) Feng, J.; Tan, A.; Wagner, S.; Liu, J.; Mao, Z.; Ke, X.; Zhang, P. Charge modulation and structural transformation in TaTe₂ studied by scanning tunneling microscopy/spectroscopy. *Applied Physics Letters* **2016**, *109*, 021901.

(20) Gao, J. J.; Si, J. G.; Luo, X.; Yan, J.; Chen, F. C.; Lin, G. T.; Hu, L.; Zhang, R. R.; Tong, P.; Song, W. H.; Zhu, X. B.; Lu, W. J.; Sun, Y. P. Origin of the structural phase transition in single-crystal TaTe₂. *Phys. Rev. B* **2018**, *98*, 224104.

(21) Wei, L.-L.; Sun, S.-S.; Sun, K.; Liu, Y.; Shao, D.-F.; Lu, W.-J.; Sun, Y.-P.; Tian, H.-F.; Yang, H.-X. Charge Density Wave States and Structural Transition in Layered Chalcogenide TaSe_{2-x} Te_x. *Chinese Physics Letters* **2017**, *34*, 086101.

(22) Battaglia, C.; Cercellier, H.; Clerc, F.; Despont, L.; Garnier, M. G.; Koitzsch, C.; Aebi, P.; Berger, H.; Forró, L.; Ambrosch-Draxl, C. Fermi-surface-induced lattice distortion in NbTe₂. *Phys Rev B* **2005**, *72*, 195114.

(23) Clerc, F.; Battaglia, C.; Cercellier, H.; Monney, C.; Berger, H.; Despont, L.; Garnier, M. G.; Aebi, P. Fermi surface of layered compounds and bulk charge density wave systems. *Journal of Physics: Condensed Matter* **2007**, *19*, 355002.

(24) van Landuyt, J.; van Tendeloo, G.; Amelinckx, S. The direct imaging of two-dimensional charge density waves and of commensurate superlattices in NbTe₂ and TaTe₂. *Physica Status Solidi (a)* **1975**, *29*, K11–K13.

(25) Chen, H.; Li, Z.; Guo, L.; Chen, X. Anisotropic magneto-transport and magnetic properties of low-temperature phase of TaTe₂. *EPL (Europhysics Letters)* **2017**, *117*, 27009.

(26) Chakravarty, D.; Kumar, P.; Ugale, V. S.; Late, D. J. Microwave-Assisted Synthesis of Few-Layered TaTe₂ and Its Application as Supercapacitor. *European Journal of Inorganic Chemistry* **2015**, *2015*, 1598–1603.

(27) Zhang, J.; Yang, B.; Zheng, H.; Han, X.; Yan, Y. Large magnetic anisotropy and strain induced enhancement of magnetic anisotropy in monolayer TaTe₂. *Physical Chemistry Chemical Physics* **2017**, *19*, 24341–24347.

(28) Xue, X.; Wang, X.; Mi, W. Electric field effects on electronic structure of tantalum dichalcogenides van der Waals TaS₂/TaSe₂ and TaSe₂/TaTe₂ heterostructures. *Applied Surface Science* **2018**, *455*, 963–969.

(29) Maaren, M. V.; Schaeffer, G. Some new superconducting group Va dichalcogenides. *Phys. Lett. A* **1967**, *24*, 645–646.

(30) Ngankeu, A. S.; Mahatha, S. K.; Guilloy, K.; Bianchi, M.; Sanders, C. E.; Hanff, K.; Rossnagel, K.; Miwa, J. A.; Breth Nielsen, C.; Bremholm, M.; Hofmann, P. Quasi-one-dimensional metallic band dispersion in the commensurate charge density wave of 1T – TaS₂. *Phys Rev B* **2017**, *96*, 195147.

(31) Bovet, M.; Popović, D.; Clerc, F.; Koitzsch, C.; Probst, U.; Bucher, E.; Berger, H.; Naumović, D.; Aebi, P. Pseudogapped Fermi surfaces of 1T – TaS₂ and 1T – TaSe₂ : A charge density wave effect. *Phys Rev B* **2004**, *69*, 125117.

(32) Chen, Y. et al. Strong correlations and orbital texture in single-layer 1T-TaSe₂. *Nat. Phys.* **2020**, *16*, 218–224.

(33) Borisenko, S. V.; Kordyuk, A. A.; Yaresko, A. N.; Zabolotnyy, V. B.; Inosov, D. S.; Schuster, R.; BÄijchner, B.; Weber, R.; Follath, R.; Patthey, L.; Berger, H. Pseudogap and Charge Density Waves in Two Dimensions. *Physical Review Letters* **2008**, *100*, 196402.

(34) Ryu, H. et al. Persistent Charge-Density-Wave Order in Single-Layer TaSe₂. *Nano Lett.* **2018**, *18*, 689–694.

(35) Zhao, J.; Wijayaratne, K.; Butler, A.; Yang, J.; Malliakas, C. D.; Chung, D. Y.; Louca, D.; Kanatzidis, M. G.; van Wezel, J.; Chatterjee, U. Orbital selectivity causing anisotropy and particle-hole asymmetry in the charge density wave gap of 2H-TaS₂. *Phys. Rev. B* **2017**, *96*, 125103.

(36) Wilson, J. A.; Yoffe, A. D. The transition metal dichalcogenides discussion and interpretation of the observed optical, electrical and structural properties. *Advances in Physics* **1969**, *18*, 193–335.

(37) Brixner, L. H. Preparation and properties of the single crystalline AB₂-type selenides and tellurides of niobium, tantalum, molybdenum and tungsten. *Journal of Inorganic and Nuclear Chemistry* **1962**, *24*, 257–263.

(38) Borisenko, S. V. “One-cubed” ARPES User Facility at BESSY II. *Synchrotron Radiation News* **2012**, *25*, 6.

(39) Borisenko, S. V.; Zabolotnyy, V. B.; Kordyuk, A. A.; Evtushinsky, D. V.; Kim, T. K.; Carleschi, E.; Doyle, B. P.; Fittipaldi, R.; Cuoco, M.; Vecchione, A.; Berger, H. Angle-resolved Photoemission Spectroscopy At Ultra-low Temperatures. *Journal of Visualized Experiments* **2012**, *68*, e50129.

(40) Flechsig, U.; Patthey, L.; Schmidt, T. Performance Measurements at the SLS Spectroscopy Beamline. AIP Conference Proceedings. 2004.

(41) Ceperley, D. M.; Alder, B. J. Ground State of the Electron Gas by a Stochastic Method. *Physical Review Letters* **1980**, *45*, 566–569.

(42) Kresse, G.; FurthmÃijller, J. Efficient iterative schemes for a initio total-energy calculations using a plane-wave basis set. *Physical Review B* **1996**, *54*, 11169–11186.

(43) Kresse, G.; Joubert, D. From ultrasoft pseudopotentials to the projector augmented-wave method. *Physical Review B* **1999**, *59*, 1758–1775.

(44) Smidstrup, S. et al. QuantumATK: an integrated platform of electronic and atomic-scale modelling tools. *J. Phys.: Condens. Matter* **2019**, *32*, 015901.

(45) Schlipf, M.; Gygi, F. Optimization algorithm for the generation of ONCV pseudopotentials. *Computer Physics Communications* **2015**, *196*, 36–44.